Chemically architectured alloys: How interphase width influences the strengthening

Diaa Mereib, Judith Monnier, Loïc Perrière, Benjamin Villeroy, Mathilde Laurent-Brocq

Mereib, D., Monnier, J., Perrière, L., Villeroy, B., and Laurent-Brocq, M., Journal of Alloys and Compounds, **2022**. 904: p. 163997
https://doi.org/10.1016/j.jallcom.2022.163997

Chemically architectured alloys: how interphase width influences the strengthening

Diaa Mereib[1], Judith Monnier[1], Loïc Perrière[1], Benjamin Villeroy[1], Mathilde Laurent-Brocq[1]

[1] ICMPE, UPEC-CNRS, 2 rue Henri Dunant, 94320, Thiais, France

Corresponding author

First name: Mathilde; Family name: Laurent-Brocq
E-mail: laurent-brocq@icmpe.cnrs.fr
Phone number: +33 (0)1 56 70 30 65
Postal adress: 2-8, rue Henri Dunant (bât D) F-94320 Thiais, France

Abstract

Chemically architectured alloys are a new concept of microstructure in which two phases are separated by a 3D network of fluctuations of composition, which is called interphase, and which induces a strengthening. Chemically architectured alloys were processed by spark plasma sintering of a mixture of pure Ni and CoCrFeMnNi high entropy alloy with varying conditions. They were characterized by scanning electron microscopy coupled with energy dispersive spectroscopy and electron backscattered diffraction, microhardness and compression tests. It was shown that the width of the interphase can be decreased by decreasing the sintering temperature and increasing the applied pressure. The strengthening effect of the interphase increases when its width decreases and its volume fraction increases. The microstructure of the chemically architectured alloys can be finely controlled by the processing parameters which will permit to maximize the strengthening. Chemical architecturation is thus an efficient and tunable strengthening mechanism.

Keywords

Metals and alloys; powder processing; Strengthening mechanism; high entropy alloys

1. Introduction

In order to meet the always more demanding industrial requirements, new concepts of materials are needed [1]. One of the most difficult challenge is to overcome the compromise between mechanical strength on the one hand and ductility as well as toughness on the other hand, which have been mutually exclusive up to now [2]. In this context, the architecturation of materials is a promising strategy, which consists in introducing an intermediate scale between the microstructure and the structure [3, 4]. Moreover, it provides a much richer panel to solve complex multi-criteria requirements than the ones provided by conventional microstructural or shape optimization alone [3, 5, 6]. Powder metallurgy, including spark plasma sintering or additive manufacturing [7], is the preferred processing path for achitectured materials. In functionally graded materials, one parameter of the microstructure varies at the macroscopic scale to meet the different requirements of the surface and the center of the piece [8-10]. A gradient is thus formed between the surface and the bulk. The varying parameter can be, for instance, the volume fraction of a hardening phase [11], the nature of the phases in presence as done in graded steels [3, 12] or the grain size [13]. In bi- or multi-modal polycrystals, the grain size also varies in a controlled way at the meso-scale [14, 15]. In lattice materials, the crystal microstructure of metals and alloys is mimicked at the macroscale, inducing a controlled network of porosity [16, 17]. Those strategies have successfully resulted in new combinations of strength and ductility.

Here, a new strategy of architecturation is proposed, with the same objective of combining mechanical strength and ductility: fluctuations of composition at the meso-scale. The idea of composition fluctuations is inspired from the early stages of spinodal decomposition, in which chemical gradients are present between the two phases in formation, but at the nanoscale. Spinodal microstructures can induce a very high strengthening [18, 19], because of a coherency strain related mechanism [20, 21]. But they also present several drawbacks, including a processing difficult to control and a risk of embrittlement [19, 22, 23].

To avoid these drawbacks, a new microstructure was designed to access the compositional fluctuations and was called “chemically architectured metallic alloys” [24]. The idea is to create a continuous variation between two end compositions (*i.e.*: *A* and *B*) having the same crystallographic structure. By appropriately choosing compositions *A* and *B*, the lattice parameter will significantly vary with composition, which will induce local coherency strains and, as in early-stage spinodal microstructure, will provide strengthening. At the mesoscale, the compositional fluctuations will form a 3D network. These scales of the chemical variations proposed here, which are intendedly larger than in spinodal microstructure, provide a new length scale of microstructural variation, as defined in the architecturation strategy.

In a previous work, an experimental proof of concept for a chemically architectured metallic alloy was provided [24]. Pure Ni and the equimolar High Entropy Alloy (HEA) CoCrFeMnNi were chosen for the end compositions *A* and *B*. Indeed, on the CoCrFeMn-Ni isopleth, the face centered cubic (fcc) solid solution domain ranges from pure Ni to CoCrFeMnNi for a large domain of temperature [25, 26], which is favorable to form the aimed chemical fluctuations. Moreover, the lattice misfit

between them is one of the most significant within this system [27, 28], which is favorable to induce the desired coherency strains. Then, the chemically architectured alloy was successfully processed by spark plasma sintering (SPS) of a mixture of Ni and HEA powder. The desired microstructure was characterized, evidencing especially the formation of a network of chemical fluctuations between the Ni and HEA domains, whose width was around 10 µm. These areas of chemical fluctuations were called interphase, to illustrate their hybrid nature, between an interface and a phase. Most importantly, it was shown that the chemical architecturation induces a significant increase of the yield strength while maintaining the ductility.

To go further, the next step is to identify the key microstructural parameters controlling the strengthening effect in the chemical architectured material and to propose a strategy to maximize it. Consequently, the objective of this study is to produce a range of (HEA+Ni) chemically architectured alloys with varying interphase width, allowing to determine the influence of this parameter on the mechanical properties. To do so, the SPS parameters were made to vary. The challenge is to combine a full densification with a limited interphase growth. Then the samples were characterized by scanning electron microscopy (SEM) coupled with energy dispersive spectroscopy (EDS) and electron back scattered diffraction (EBSD), hardness measurements and compression tests. Finally, the contributions to strengthening of each mechanism and each phase were calculated and discussed.

2. Experimental

Powder metallurgy has been selected as an efficient process for chemically architectured alloy in a previous study [24]. The main steps are recalled. The equimolar CoCrFeMnNi powder was produced by gas atomization at Nanoval GmbH & Co. The powder was efficiently treated in a hydrochloric acid solution to reduce the surface oxides. A high purity (> 99.996 wt. %) commercial Ni powder was used. Both powders were sieved to have a powder grain size ranging from 20 to 36 µm. HEA powder grains are spherical whereas the ones of Ni are round with a significant surface roughness. It is mentioned that, despite sieving, some Ni powder grains are smaller than 20 µm. For the architectured samples, CoCrFeMnNi and Ni sieved powders were mixed with a 1:1 mass ratio during 30 minutes in a Turbula® mixer (WAB Group, Switzerland).

SPS was chosen as sintering technique. DR SINTER LAB Spark plasma sintering system (model Fuji 515-S) apparatus, of the “Plateforme Ile-de-France de Frittage” was used in this study. A 10 mm diameter die was lined with graphite paper Papyex®. Around 2 g of powder was sintered, which results in pellets with an approximate thickness of 3 mm. The temperature is measured by a K-type thermocouple inserted into the die wall. The mixture of CoCrFeMnNi and Ni powders were consolidated at a maximum temperature T_{max} of either 500, 600, 700 or 850°C. To obtain in any case a satisfying densification (porosity < 1 vol. %), the die, the applied pressure and the heating rate were adapted (Table 1, section 3.1). For all samples, sintering was performed under vacuum. The temperature was increased up to the maximum temperature, then an uniaxial pressure was applied to the pellet and both the pressure and the maximum temperature were maintained for a duration of 15 minutes. Afterwards, load and temperature were decreased in a few minutes. The CoCrFeMnNi and the Ni powders alone were also sintered at 850°C for reference.

The samples are named (X)-ST where (i) X indicates the composition and is either (HEA+Ni) for chemically architectured alloys, HEA or Ni for reference samples, (ii) S stands for sintered and (iii) T indicates the sintering temperature expressed in °C. They are listed in Table 1.

The surface of sintered pellets was mechanically polished to remove the surface layers which may contain undesired carbides. Indeed, it was already shown that CoCrFeMnNi is very sensitive to carbon contamination [29], including from the mold and paper during SPS [30]. The density of the sintered pellet is determined using the buoyancy technique, which is based on the Archimede's principle. Samples, including references, were characterized by X-Ray Diffraction (XRD) on a PANAlytical X'Pert Pro diffractometer using the Co-K_α radiation at a wavelength of 0.178897 nm. The microstructure of the samples was further studied using a Zeiss Merlin Field Emission SEM mainly in backscattered electron (BSE) mode. The SEM is coupled with an EDS and an EBSD detector from Oxford Instruments. Both detectors are driven by AZtec operating system.

To calculate the width of the interphase, 10 EDS profiles per sample were collected along lines which are perpendicular to HEA/Ni interfaces. The electron energy was 15 keV, the step size was 150 nm, and the length of the line is around 30 µm. The profiles were analyzed with the following procedure. The difference Δ between the maximum $[C]_{max}$ and minimum $[C]_{min}$ of the concentration of element *C* was calculated. Then the points with a concentration equal to $[C]_{max} - 0.05 \times \Delta$ and $[C]_{min} + 0.05 \times \Delta$ were determined. The interphase width is defined as the difference between the abscissa of these two points. This procedure is illustrated in our previous study [24]. The interphase width is calculated for each element (Table S 1) and then the final width is the average of those five values.

EDS mappings with an area of 144×108 µm² and a pixel width of 0.56 µm were recorded. Each pixel corresponds to a high-resolution spectrum, from which a precise composition can be calculated. Similarly, to the procedure used to determine the gradient width, a pixel was attributed to the interphase if its Ni content was in between $[C]_{max} - 0.1 \times \Delta$ and $[C]_{min} + 0.1 \times \Delta$. If it was larger than $[C]_{max} - 0.1 \times \Delta$, it was attributed to the Ni phase and in the latter case, to the HEA phase. Afterwards, phase maps were reconstructed. The same procedure was applied by considering the Co, Cr, Fe and Mn content. The volume fraction of the interphase was calculated in each case. The given volume fraction and the corresponding uncertainty are respectively the average and the standard deviation of the volume fraction determined for each element content.

Moreover, areas with a dimension of 230×170 µm² were mapped by EBSD coupled with EDS, with a step size of 200 nm and an electron energy of 20 keV. This coupling permits to distinguish the HEA and Ni phases based on their difference of composition. This would not have been possible by a standard EBSD characterization because the HEA and Ni phases have the same crystallographic structure with too close lattice parameters. On EBSD mapping, grain boundaries were defined as lines with a crystallographic disorientation of at least 10° and Σ3 boundaries were excluded. The grain size is the average of the size of such detected grains.

Next, the mechanical properties were studied. The hardness of all samples was measured using a FM-700 Vickers micro-indenter at a 1000 gf load and 12 s dwell time. The given hardness and uncertainty are respectively the average and standard deviation over at least 10 measurements. Afterwards, compression tests were performed. Since machining of compression specimen in the SPS pellet is complex, (HEA+Ni)-S600, (HEA+Ni)-S850 and the reference samples HEA-S850 and Ni-S850 were chosen to be studied by this method. Specimen were cut into parallelepiped with a height

of 4 mm and a section of 2.5×2.5 mm², giving an aspect ratio of 1.5. The higher dimension of the parallelepiped is put perpendicular to the height of the pellet. Like this, with a pellet diameter of 10 mm, a height of 4 mm is possible. The compression faces of the samples were grounded perfectly parallel by mechanical polishing to ensure stress uniaxiality. For each selected composition and sintering conditions, two specimens were tested. An Instron 5966 machine with a maximum force of 10 kN was used. Samples were compressed at a constant ram speed that provided an initial strain rate of 0.001 s^{-1}. When a force of 6000 N was reached, the test was interrupted. The linear compliance of the machine was experimentally determined to be of 3.8×10^{7} $N.m^{-1}$ in the force range of 0 to 6000 N. Strains were accordingly corrected. The yield strength was determined at 0.2 % of plastic strain.

Table 1 : List of the sintered samples. The optimized SPS conditions are given. The volume fraction porosity was measured by the Archimede's method.

Sample name	SPS conditions					Volume fraction of porosity (%)
	Starting powders	Maximum temperature T_{max} (°C).	Heating speed (°C.min^{-1})	Pressure P_{max} (MPa)	Type of mold	
(HEA+Ni)-S500	HEA, Ni	500	300	500	WC/Co*	0.98
(HEA+Ni)-S600	HEA, Ni	600	100	400	WC/Co*	0.30
(HEA+Ni)-S700	HEA, Ni	700	100	200	Graphite	0.30
(HEA+Ni)-S850	HEA, Ni	850	100	100	Graphite	0.79
HEA-S850	HEA	850	100	100	Graphite	0.14
Ni-S850	Ni	850	100	200	Graphite	0.70

**WC/Co: tungsten carbide mold doped with Co*

3. Results

3.1. Processing of chemically architectured alloys

In this study, it is intended to process chemically architectured alloy with various widths of interphase, equal or lower than 10 µm. The first step consists in identifying the appropriate sintering conditions to control the interphase width while keeping the volume porosity lower than 1 %. The starting point is the SPS conditions identified in a previous study [24] and which permit to process a dense enough chemically architectured alloy with an interphase width of 10 µm. Those conditions are the following: using a graphite die, the temperature was increased up to T_{max} = 850°C with a heating speed of 100°C.min^{-1}, then a pressure P_{max} of 100 MPa was applied, both the maximum temperature and the pressure were maintained for either 5 or 15 minutes. To limit species solid diffusion [31] and thus interphase width, duration or temperature of the plateau has to be decreased. Since the width of 10 µm for the interphase was already formed after a plateau of only 5 minutes, duration was rejected as a possible parameter to decrease interphase width. Thus, it was

chosen to process chemically architectured alloys for T_{max} = 500, 600, 700 and 850°C. First, other SPS parameters were kept constant. However, the obtained pellets were not dense enough. Second, applied pressure was progressively increased until a satisfying density was obtained. For T_{max} = 700°C, the selected plateau pressure was 200 MPa. For T_{max} = 600°C, a pressure of 400 MPa was needed. Since the graphite die could not stand such a high pressure, a tungsten carbide die was used instead. For T_{max} = 500°C, the pressure was increased again up to 500 MPa and, to improve the reproducibility, the heating rate to reach the plateau was increased up to 300°C.s^{-1}.

CoCrFeMnNi and pure Ni powders were also sintered alone, for reference. The objective is to process materials with a similar microstructure than the chemically architectured alloy but without an interphase. CoCrFeMnNi was densified with the same conditions than the chemically architectured alloy. At 850°C, a volume fraction of porosity of 0.14 % was obtained. However, at 700°C and 500°C, volume fractions of porosity of respectively 1.4 and 7.2 % were measured. Such samples were not considered as suitable, especially for mechanical characterization. For Ni powder, for the sintering at 850°C, it was necessary to increase the pressure up to 200 MPa to obtain a satisfying densification. Sintering at lower temperature was not tested. Thus, the mixture of CoCrFeMnNi and Ni powders is more favorable for sintering than CoCrFeMnNi or Ni powders alone and satisfying densification can be obtained for the lower sintering temperature for the first one. Consequently, it was possible to process reference samples only for T_{max} = 850°C.

The optimized SPS conditions are summarized in Table 1 together with the volume porosity. As desired and thanks to the tuning of the sintering maximum temperature and pressure as well as the type of mold, the volume porosity is lower than 1 for all samples.

3.2. Microstructure characterization

A microstructure characterization of all optimized samples (listed in Table 2) was performed by SEM coupled with EDS and EBSD. The one of (HEA+Ni)-S600 is depicted in Figure 1 while the ones of the other samples are given in supplementary materials (Fig. S 1, Fig. S 2 and Fig. S 3). All chemically architectured alloys share some common features: they exhibit a homogeneous distribution of round particles, which are the HEA phase, in a percolating matrix, which is the Ni phase (Figure 1a). Some agglomeration of the particles is locally observed. There is no porosity spotted on the surface of the sample which agrees with the fully dense aspect. On EDS mapping (Figure 1 (b-f)), especially for Mn, the blurred interfaces are indicative of the interphase.

To characterize in more details the interphase, SEM-EDS line profiles were also performed. Figure 2(a) and (b) shows an example of such a line profile measured for (HEA+Ni)-S600 with the corresponding SEM-BSE image. When starting from the left in the Ni phase, the concentration of Ni gradually and continuously decreases while the concentration of Co, Cr, Fe and Mn increases. This area of composition variation corresponds to the interphase. Afterwards, the concentration of each element reaches 20 at. %, which corresponds to the equimolar CoCrFeMnNi, and stabilizes. More precisely, it is noticed that the composition evolution of Co, Cr and Fe is very similar while the one of Mn is different. Indeed, it varies with a smaller slope and on a larger length. These qualitative features are shared by all the samples. Nevertheless, as illustrated for Co on Figure 2(c), the interphase width appears as different in each sample: it decreases with the sintering temperature.

The average interphase width varies from 9.8 µm for T_{max} = 850°C down to 2.4 µm for T_{max} = 500°C (Table 2 and Figure 3 (a)). In between, it has a value of 6.3 and 3.4 µm respectively for T_{max} = 700 and 600°C. Thus, decreasing the maximum sintering temperature is an efficient strategy to control the interphase width, as intended. It is recalled that, in the studied samples, when the sintering temperature changes, other sintering parameters vary too. For the sake of simplicity, those last ones are not always recalled. On Figure 2(c), it can also be observed that the slope of the composition variation increases when the sintering temperature decreases. To quantify this tendency, an average chemical gradient is calculated. It varies from 2 at. %/µm in (HEA+Ni)-S850 up to 8 at. %/µm in (HEA+Ni)-S500. (Table 2). This is expected since the composition of phases on each side of the interphase is the same in all samples while the width of the interphase varies.

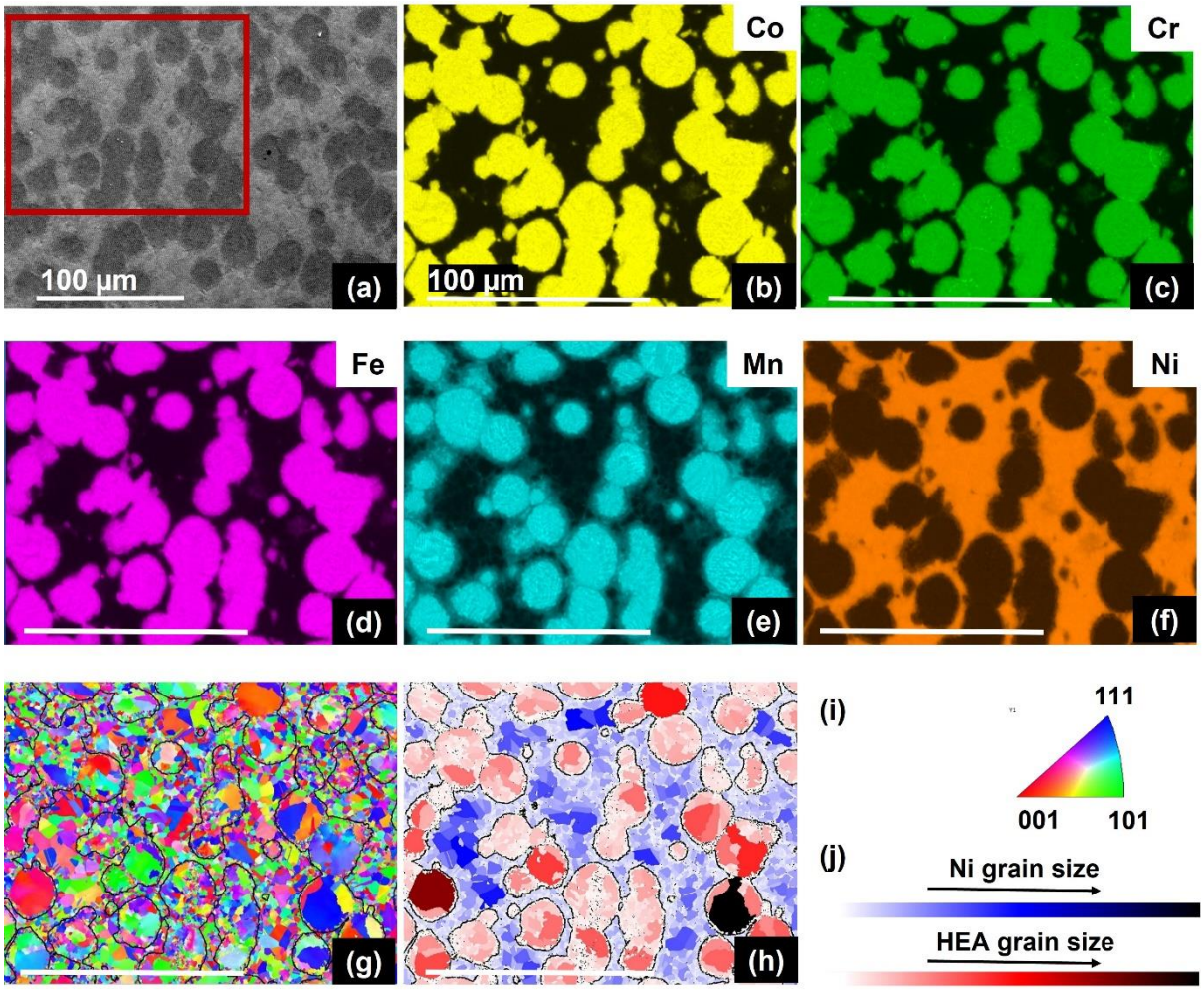

Figure 1 : Microstructural characterization of the chemically architectured alloy (HEA+Ni)-S600 (a) SEM image in BSE mode. The red square indicates the area of EDS and EBSD mapping. (b, c, d, e and f) EDS mapping of Co, Cr, Fe, Mn and Ni respectively. (g) EBSD orientation map and grain boundaries (black lines). The corresponding standard stereographic triangle is given in (i). (h) EBSD grain size map and grain boundaries (black lines). The color legend is given in (j). The scale is the same for (b) to (h).

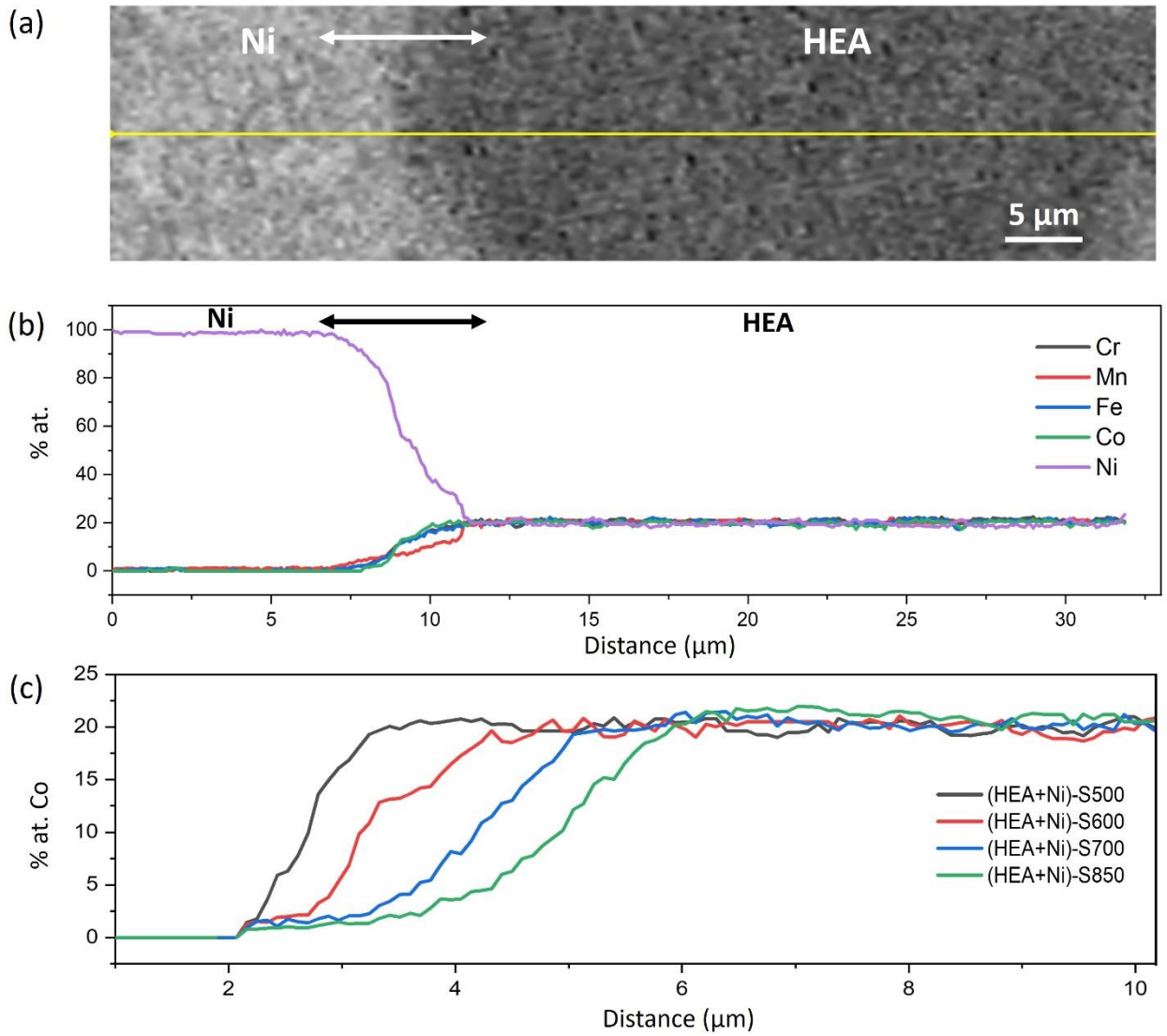

Figure 2 : Measurements of interphase width in chemically architectured alloys by SEM-EDS line profiles. (a) SEM image in BSE mode of (HEA+Ni)-S600. The yellow line localizes the EDS profile which is plotted in (b). The arrows indicate the interphase. (c) EDS line profiles of Co through the interphase in (HEA+Ni)-S500, (HEA+Ni)-S600, (HEA+Ni)-S700 and (HEA+Ni)-S850.

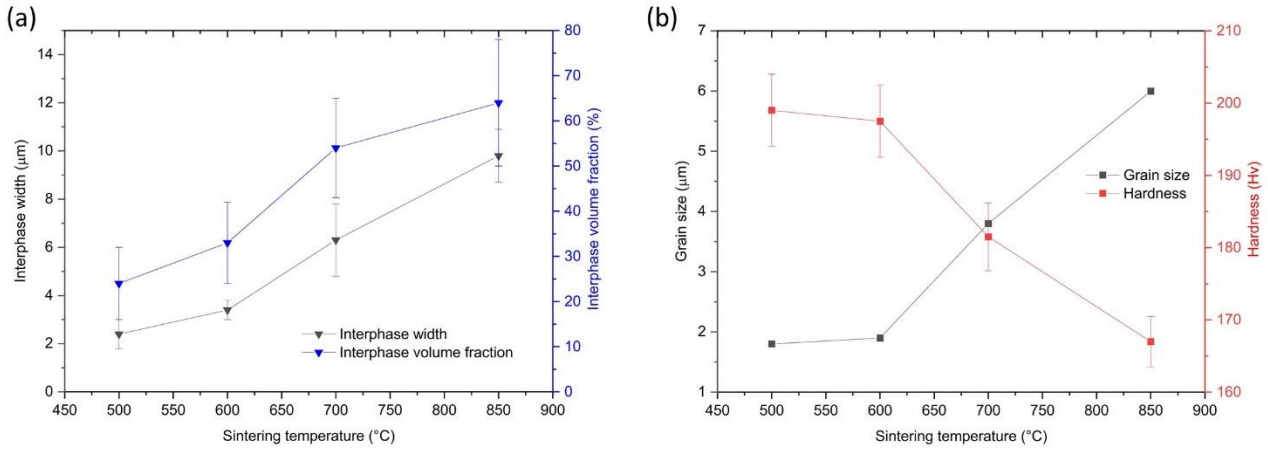

Figure 3 : Evolution of (a) the width and volume fraction of the interphase and of (b) the grain size and hardness with the sintering temperature in chemically architectured alloys. The width and volume fraction of the interphase were measured by SEM-EDS while the grain size and hardness were measured by EBSD and Vickers microhardness respectively.

Next, by analyzing EDS mapping, the phase volume fractions were calculated. Here again, it varies with the sintering temperature. The interphase volume fraction increases from 24 % in (HEA+Ni)-S500 up to 64 % in (HEA+Ni)-S850 (Table 2 and Figure 3(a)). These very high values justify the fact that the interphase cannot be treated as an interface. It can be noticed that Ni volume fraction is significantly lower than the one of HEA for (HEA+Ni)-S500 and (HEA+Ni)-S600. It means that the interphase grows preferentially towards the Ni phase. In (HEA+Ni)-S850, the volume fractions of HEA and Ni phases are equal, meaning that the interphase growth has rebalanced. The corresponding phase distributions are reconstructed in Figure 4. It provides an easier visualization of the interphase localization compared to the EDS mapping (Figure 2(b-f)). First, it is observed that HEA round particles are entirely surrounded by interphase, except where HEA particles are in contact. Second, with the increase of sintering temperature and, as a consequence with the increase of interphase width, interphase areas around different HEA particles overlap more and more. In (HEA+Ni)-S850, this overlap is so extended that it becomes more accurate to consider the interphase as the percolating matrix surrounding both HEA and Ni phases.

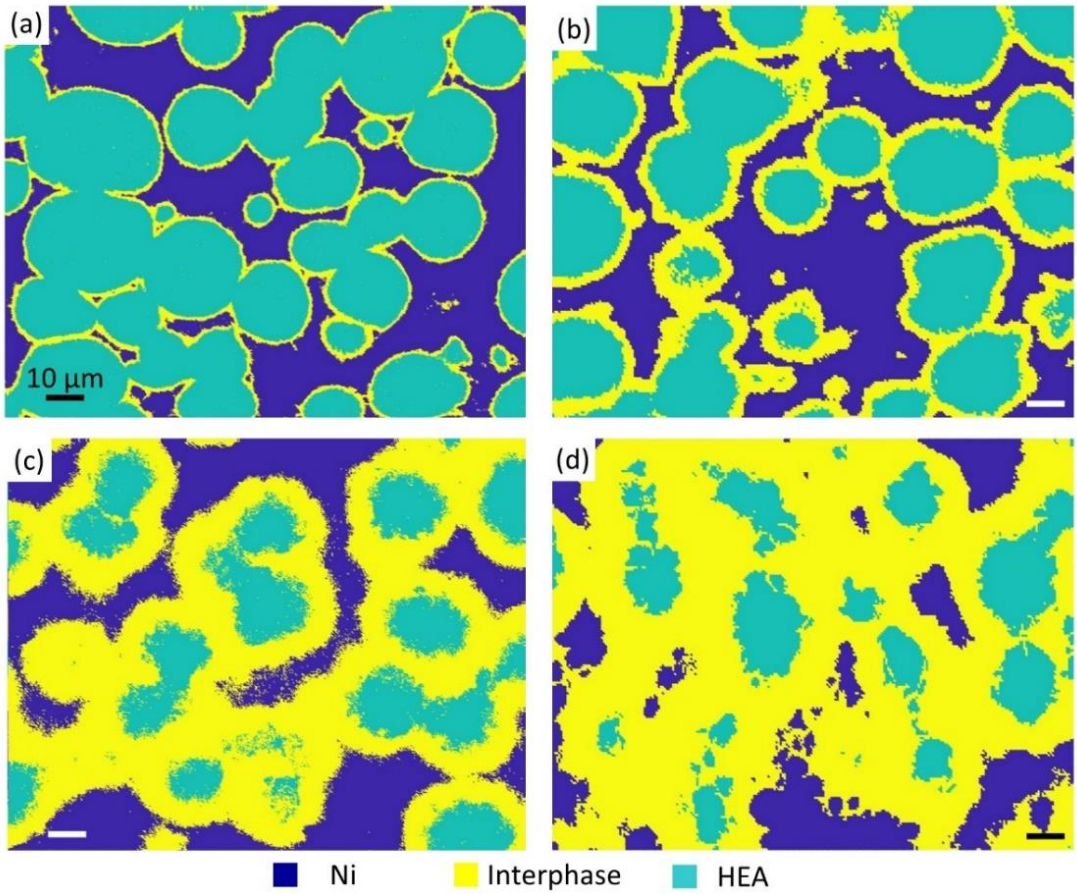

Figure 4 : Phase maps for (a) (HEA+Ni)-S500, (b) (HEA+Ni)-S600, (c) (HEA+Ni)-S700 and (d) (HEA+Ni)-S850. Those maps were reconstructed based on EDS mapping analysis. The scale is the same from (a) to (d).

As intended, decreasing the sintering temperature has resulted in a change of the width and, consequently, of the volume fraction as well as the average chemical gradient of the interphase. But

it has also changed the grain size. It is recalled that grains are understood as areas inside which the crystallographic orientation is constant and which are delimited by grain boundaries. Figure 1(g) and (h) shows EBSD maps for (HEA+Ni)-S600. According to Figure 1(g), there is no preferential crystallographic grain orientation in the HEA or Ni phases and no specific disorientation is observed at the interphase. Moreover, according to Figure 1(h), grain size is similar in HEA and Ni phases. These features were observed in all the architectured alloys. The average grain size is given in Table 2 and plotted on Figure 3(b). It decreases with sintering temperature from 7 µm in (HEA+Ni)-S850 down to 1.8 µm in (HEA+Ni)-S500. It is mentioned that the grain size of (HEA+Ni)-S500 and (HEA+Ni)-S600 is very close.

Finally, chemically architectured alloys were characterized by XRD (Figure 5). The HEA and Ni phases were indexed on the patterns of the references samples HEA-S850 and Ni-S850 [24]. It is recalled that both are face-centered cubic (fcc) phases. Those values were reported on Figure 5 (red and blue lines respectively). For (HEA+Ni)-S500, the peaks of HEA on the one hand and of Ni on the other hand can be easily identified. For the other samples, when the sintering temperature increases, the peaks enlarge, their maximum slightly shift until they merge into a broad and irregular peak for (HEA+Ni)-S850. The angular domain between the HEA and Ni peaks (more visible on Figure 5(b)) can be attributed to the interphase. The diffraction intensity of this domain increases from (HEA+Ni)-S500 to (HEA+Ni)-S850 which is in qualitative agreement with the increase of the interphase volume fraction measured on EDS mapping (Table 2). To quantitatively determine this evolution from the XRD pattern, the difference of X-ray absorption between HEA and Ni needs to be calculated. This was done in [32] and was found in quantitative agreement with EDS analysis. Finally, it is underlined that all the diffraction peaks of chemically architectured alloys can be attributed to the HEA and Ni phases (Figure 5(a)). In other words, no other unwanted phases were detected by XRD.

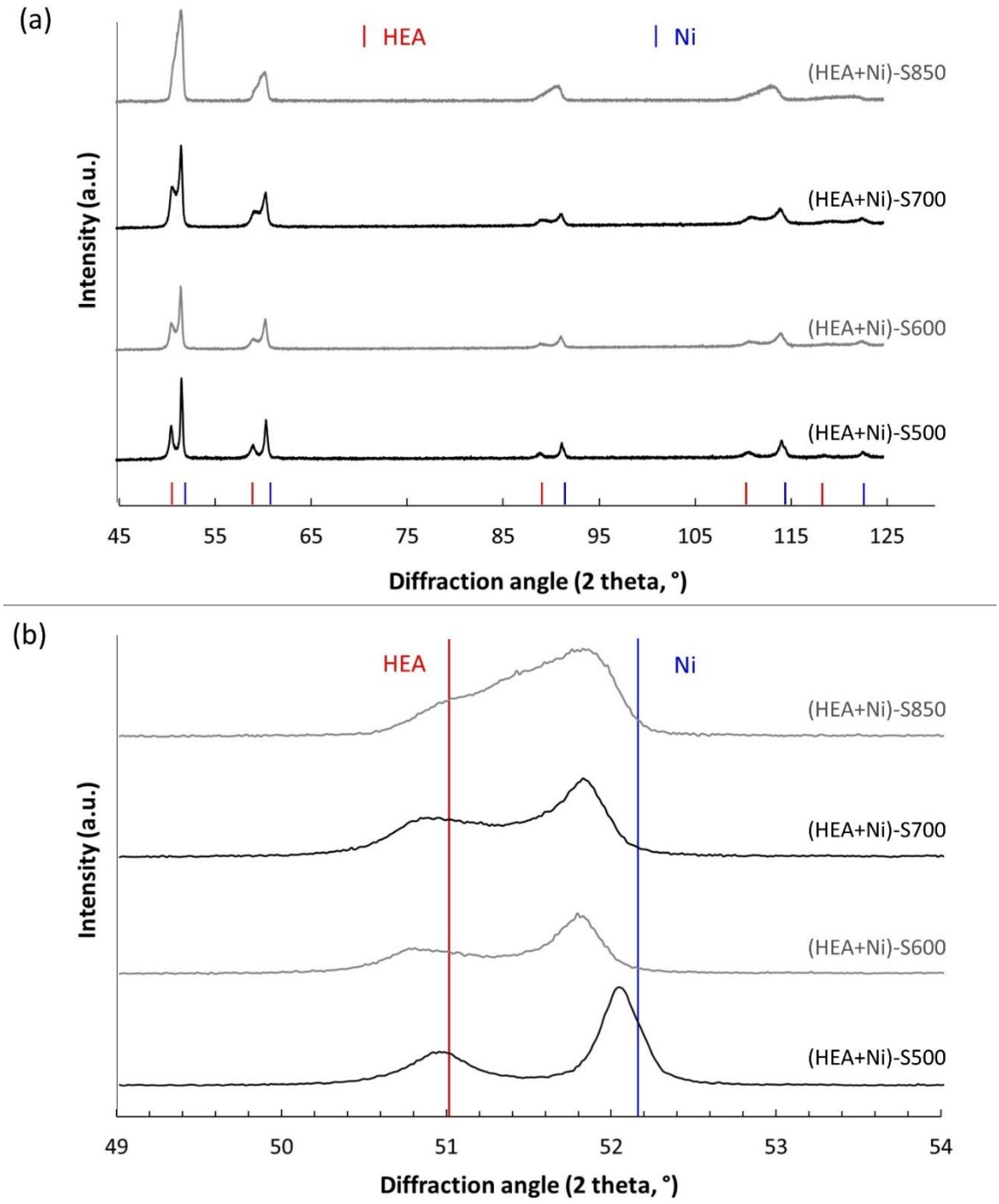

Figure 5 : X-ray diffraction patterns of chemically architectured alloys. (a) Complete patterns, (b) zoom on the first two peaks. Red and blue lines indicated the diffraction peaks of the HEA and Ni phases.

To summarize, when decreasing the sintering temperature while increasing the pressure, the interphase width and volume fraction as well as the grain size decrease. Since several sintering parameters were made to vary together, it is not possible to separate their influence on the microstructure evolution. This does not compromise the objective of this study, which is to experimentally study chemically architectured alloys with various microstructures, especially various gradient width, and to determine how it influences the strengthening. Next, the mechanical properties are measured.

Table 2: Results of the microstructural and mechanical characterization of the sintered samples. The grain size was measured by EBSD. The width and volume fraction of the interphase were measured by SEM-EDS. The hardness and yield strength were measured by micro-indentation and compression tests respectively. The given uncertainties are the standard deviation of the measurements.

Sample name	Grain size (µm)	Phase volume fraction (%)			Interphase width (µm)	Chemical gradient (at. %/µm^{-1})	Hardness (HV)	Yield strength (MPa)
		HEA	Ni	Interphase				
(HEA+Ni)-S500	1.8 ± 1.4	49 ± 7	27 ± 2	24 ± 8	2.4 ± 0.6	8	199 ± 5	-
(HEA+Ni)-S600	1.9 ± 1.5	39 ± 6	28 ± 4	33 ± 9	3.4 ± 0.4	6	197 ± 4	450 ± 14
(HEA+Ni)-S700	3.8 ± 2.5	19 ± 4	24 ± 8	54 ± 11	6.3 ± 1.5	3	181 ± 4	-
(HEA+Ni)-S850	7 ± 3.5	18 ± 7	18 ± 8	64 ± 14	9.8 ± 1.1	2	165 ± 4	315 ± 5
HEA-S850	5 ± 3	×	×	×	×	×	183 ± 1	381 ± 6
Ni-S850	6 ± 2	×	×	×	×	×	88 ± 1	120

"-" indicates that the measurement was not performed. "×" indicates that this data is not relevant.

3.3. Mechanical properties

To discover the effect of the microstructure evolution in the architectured alloys processed at different temperatures on the mechanical properties, Vickers microhardness and compression test were performed. The hardness of both architectured and reference samples are given in Table 2 and plotted in Figure 3 (b). A hardness of 165 HV was measured on (HEA+Ni)-S850. This value is in between the ones of the corresponding reference samples HEA-S850 and Ni-S850 whose hardness is of 183 and 88 HV respectively. Pure sintered Ni is significantly softer than pure HEA. The architectured alloy hardness is closer from the one pure HEA than the one of pure Ni. When the sintering temperature decreases, the hardness of architectured alloy increases. It has a value of 181, 197 and 199 HV respectively for (HEA+Ni)-S700, (HEA+Ni)-S600 and (HEA+Ni)-S500. Thus, the hardness of pure HEA sintered at 850°C is overcome when the sintering temperature is equal to 600 or 500°C. It is underlined that, when decreasing the sintering temperature, both the interphase width and the grains size evolve (section 3.2) and both are likely to influence the hardness. The contribution of each feature of the microstructure to the strengthening will be discussed later (section 4).

Next, compression tests were performed on selected samples with different interphase characteristics: (HEA+Ni)-S850 whose exhibit the largest interphase width and volume the fraction;

the corresponding reference samples HEA-S850 and Ni-S850; (HEA+Ni)-S600 with a small interphase width and volume fraction. The last one was preferred to (HEA+Ni)-S500 whose porosity volume fraction was higher (0.98 % compared to 0.3 % for (HEA+Ni)-S600), which could be detrimental to mechanical properties. It is recalled that there is no reference samples at 600°C because it was not possible to process them with a satisfying densification (section 3.1). The engineering stress-strain curves are plotted on Figure 6. The yield strength, determined at 0.2 % of plastic deformation, is given in Table 2. (HEA+Ni)-S850 has a yield strength of 315 MPa, in between the yield strength of the reference samples. The yield strength of (HEA+Ni)-S600 reaches a higher value, of 450 MPa. This tendency is in agreement with hardness measurements. More specifically, it can be observed that the transition between the elastic and plastic zone is smoother for the architectured alloy than for the reference alloys. Indeed, when a two-phase material is submitted to an external stress [33], in a first stage, both phases deform elastically. In a second stage, the applied stress reaches the yield stress of the softer phase, here Ni, which starts to plastically deform while the harder phase, here HEA, continues to elastically deform. A discontinuity of strain appears at the boundaries of both phases, which produces an internal stress and aids the onset of plastic deformation in the harder phase, at a lower applied stress than the yield stress of the harder phase. In the third stage, both phases plastically deform. The smooth transition between elastic and plastic zone observed on stress-strain curves of chemically architectured alloys corresponds to the second stage.

Second, it can be observed for all samples that the stress continuously increases with strain, which indicates a significant strain hardening. More specifically, the slope of the stress-strain curves for (HEA+Ni)-S850 and HEA-S850 are similar, while the one of Ni is slightly smaller. It indicates that, at a given sintering temperature, the chemical architecturation maintains the highest strain hardening of the single-phase materials. However, the strain hardening of (HEA+Ni)-S600 appears to be slightly smaller than the one of (HEA+Ni)-S850. Since both the interphase and the grains have evolved with sintering temperature, it is not possible to sort out which one is the cause of the strain hardening decrease.

Finally, a deformation larger than 20 % was reached for all samples. It was considered that compression test is not appropriate to measure rupture and so the compression tests were interrupted at a given force. Nevertheless, it can be concluded that architectured alloys, like the reference samples, advantageously exhibit a large ductility.

To summarize, when decreasing the sintering temperature while increasing the pressure, the hardness and the yield strength of architectured alloys increases while maintaining a significant ductility. Now the contribution of the interphase and the influence of its characteristics on strengthening will be discussed.

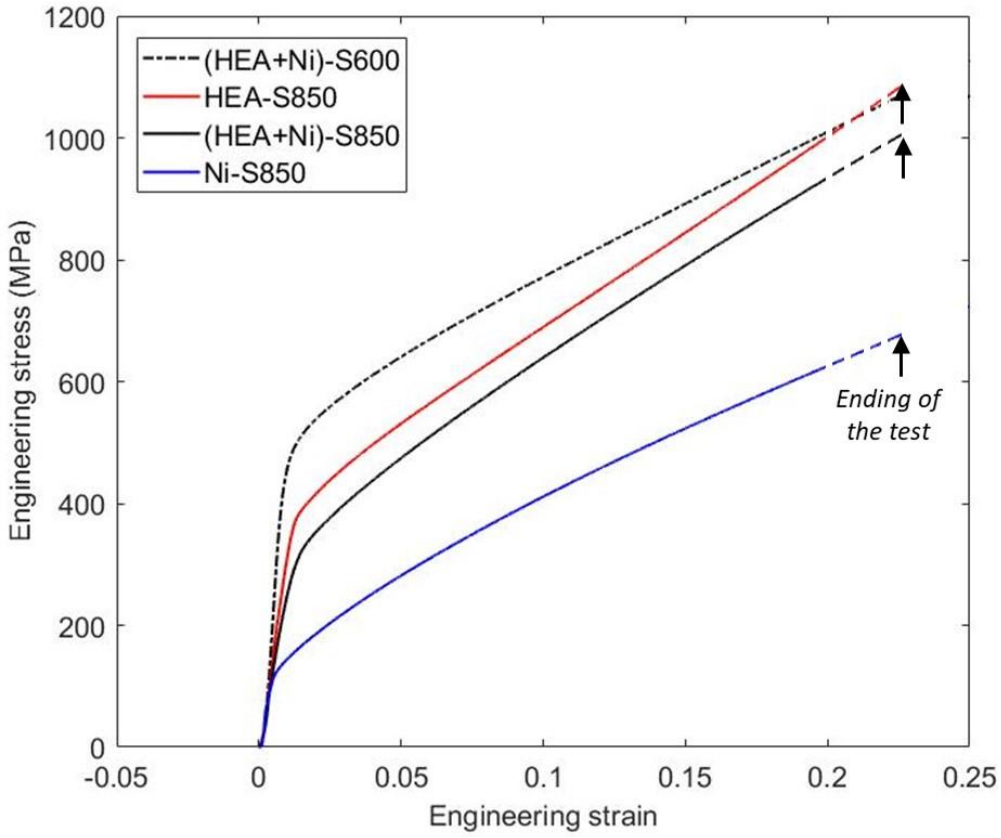

Figure 6 : Engineering stress-strain curves of compression tests on reference single phase HEA (red), reference single phase Ni (blue) and on chemically architectured alloys sintered at 850°C (black) or 600°C (black dashed). All tests were ended before rupture

4. Discussion

It was shown that it is possible to decrease the interphase width by decreasing the sintering temperature T_{max} and increasing the sintering pressure P_{max}. Concomitantly, other parameters of the microstructure evolve, like the interphase volume fraction and the grain size. All these microstructure changes result in an increase of the yield strength. The objective of this part is to sort out the contribution of each strengthening mechanism, which are influenced by the evolution of the microstructure, with a focus on the contribution of the interphase.

To do so, the chemically architectured alloys are considered as three-phase materials and the contribution of the interphase is treated similarly as the one of HEA or Ni phase. The yield strength of the three-phase material is calculated according to the Voigt estimate, in which uniform strain is assumed in the whole material [34, 35]. Then, the yield strength is equal to the sum of the yield strength of each phase, balanced by its volume fraction. Thus, the expression of the total yield strength σ_y becomes:

$$\sigma_y = f_{Ni} \cdot \sigma_{Ni} + f_{HEA} \cdot \sigma_{HEA} + f_I \cdot \sigma_I = \Sigma_{Ni} + \Sigma_{HEA} + \Sigma_I \quad (1)$$

Where f_j and σ_j are respectively the volume fraction and yield strength of the phase j, with j being either HEA, Ni or the interphase (I). The total strengthening contribution of phase j is written Σ_j.

It is mentioned that the Voigt approximation is not always in agreement with experimental data and is often proposed as an upper limit of the yield strength of multi-phase materials [34, 35].

Nevertheless, Fe-Cr-Ni alloys, composed of austenite and ferrite in varying proportions, including 0.5 of each, were processed and characterized by tensile tests [33]. The determined yield strength was in quantitative agreement with the Voigt estimate. Those Fe-Cr-Ni alloys have the specificity that the two phases have similar elastic constants. The chemically architectured alloys have several common points with those two-phase Fe-Cr-Ni alloys: the chemical composition is close; the crystalline structure is face centered cubic as for the austenite; and the elastic constants of Ni and HEA are similar [36], as it is the case for austenite and ferrite. Thus, the Voigt estimate is likely to be appropriate. Otherwise, its yield strength will be overestimated and, as a result, the effect of the chemical architecturation will be underestimated and not overestimated.

The contributions of HEA, Ni and the interphase can be decomposed further to sort out the effect of each strengthening mechanism. The total yield strength σ_y is then written as:

$$\sigma_y = f_{Ni} \cdot (\sigma_{Ni,SS} + \sigma_{Ni,GB}) + f_{HEA} \cdot (\sigma_{HEA,SS} + \sigma_{HEA,GB}) + f_I \cdot (\sigma_{I,SS} + \sigma_{I,GB} + \sigma_{I,grad}) \quad (2)$$

Where $\sigma_{j,SS}$ and $\sigma_{j,GB}$ are the strengthening due respectively to the lattice (solid solution in HEA and the interphase or Peierls stress in Ni) and the grain boundary in the phase j. A third term, $\sigma_{I,\,grad}$, is added in the interphase contribution. It will quantify the effect of the new strengthening mechanism which is induced by the fluctuations of composition within the interphase and which is the main focus of this study.

The reference materials HEA-S850 and Ni-S850 are appropriate to determine the yield strength for a sintering temperature of 850°C. Unfortunately, it was not possible to process reference materials for the other sintering temperatures. As already pointed out in [24], the yield strength of HEA-S850 and Ni-S850 are in quantitative agreement with Otto *et al.* [37] and Keller *et al.* [38], in which Hall & Petch coefficients were determined respectively for CoCrFeMnNi and pure Ni. Knowing the grain size of each chemically architectured sample thanks to the EBSD measurements (Table 2), those coefficients are used to calculate $\sigma_{j,SS}$ and $\sigma_{j,GB}$: $\sigma_{j,SS} = \sigma_{0,j}$ and $\sigma_{j,GB} = K_j/\sqrt{d}$ with $\sigma_{0,j}$ and K_j the Hall & Petch coefficients of phase j and d the grain size. $\sigma_{0,j}$ is equal to 14 and 125 MPa respectively for Ni and CoCrFeMnNi, while K_j is equal to 180 and 494 MPa.$\mu m^{-1/2}$ respectively for Ni and CoCrFeMnNi [37, 38].

The calculation of the interphase contribution is less obvious. The following approach was chosen. First, an analytical model of solid solution strengthening (SSS) developed for high entropy alloy was used [39]. This model depends on the chemical composition. It was applied to single-phased HEA of different compositions within the Co-Cr-Fe-Mn-Ni system and was found in good agreement with experimental data [27]. The detailed equations are given in [27, 39]. They use input data, which gather elastic constants and atomic volumes. In Bracq *et al.* [27], four datasets were tested and validated. Here, the SSS was calculated with all four dataset and then averaged. The given uncertainty is the standard deviation of the calculations with the different datasets (Table 3). To apply the SSS model, the interphase was considered as a succession of small volumes of single-phase alloy, with varying composition. Based on the Varvenne *et al.* model [39], the SSS was calculated for each small volume, whose composition was determined based on the EDS mapping (Figure 1(b-f)). The length of one volume was taken as 0.56 µm. This is small enough to have at least five volumes

through the interface. Since the lattice parameter of CoCrFeMnNi is 3.600 Å [26], this is large enough to contain more than 104 atoms and thus preserve the random nature of a solid solution. The calculated SSS of each small volume is mapped in Fig. S 4.

Second, the grain boundary contribution $\sigma_{I,GB}$ was calculated. To do so, the grain size and the Hall & Petch coefficient K_j are needed. The average material grain size, in other words, the size used for $\sigma_{HEA,GB}$ and $\sigma_{Ni,GB}$, was used. The coefficient K_j strongly depends on the composition, as it can be seen for HEA and Ni. Since this dependency is not known, it was chosen to use the same Hall & Petch coefficients as for HEA, although this is likely an overestimation. The volume fractions of each phase as determined on EDS mapping were used (Table 2).

Based on that, the mechanical contribution of the chemical gradient $\sigma_{I,grad}$ is calculated by subtracting all the other contributions to the experimental yield strength of chemically architectured alloys. This was done for (HEA+Ni)-S600 and (HEA+Ni)-S850, for which compression tests were performed.

Finally, the contributions can also be sorted out according to the strengthening mechanism accross all phases by summing the previously calculated contributions.

$$\sigma_y = \sum_{j=Ni,HEA,I} f_j \cdot \sigma_{j,SS} + \sum_{j=Ni,HEA,I} f_j \cdot \sigma_{j,GB} + f_I \cdot \sigma_{I,grad} = \Sigma_{SS} + \Sigma_{GB} + \Sigma_{grad} \quad (3)$$

Where Σ_X is the total contribution of the strengthening mechanism X, with X being either the solid solution, the grain boundary or the chemical gradient.

The calculated contributions are given in Table 3 and plotted in Figure 7. It is recalled that, for our samples, when the sintering temperature decreases, the pressure increases and the type mold changes, although this is not indicated on Figure 7. The evolution with the sintering temperature is the same for the Ni and HEA phase, with higher values for HEA than for Ni. When the sintering temperature decreases, the grain boundary contribution σ_{GB} increases while the one of solid solution σ_{SS} remains constant (Figure 7(a)). Since the volume fraction of HEA and Ni also increases when the sintering temperature decreases, the balanced contributions $\sigma_{HEA} \cdot f_{HEA}$ and $\sigma_{Ni} \cdot f_{Ni}$ significantly increases (Figure 7(b)). As a result, the total yield strength of (HEA+Ni)-S600 is larger than the one of (HEA+Ni)-S850. The evolution for the interphase is more complex. As for the Ni and HEA phases, the grain boundary contribution σ_{GB} increases while the one of solid solution σ_{SS} remains constant when the sintering temperature increases (Figure 7(a)). There is a third strengthening mechanism in the interphase: the chemical gradient $\sigma_{I,grad}$. It also significantly increases when the sintering temperature decreases: from 99 MPa to 210 MPa respectively in (HEA+Ni)-S850 and (HEA+Ni)-S600. It is recalled that the width of the interphase is thinner in (HEA+Ni)-S600 and, as a result, the average chemical gradient is larger. This means that the strengthening induced by chemical fluctuations increases with the average chemical gradient. This result is of utmost importance. However, in (HEA+Ni)-S600, the volume fraction of interphase is smaller than in (HEA+Ni)-S850. This counterbalances the increase of $\sigma_{I,grad}$ and of $\sigma_{I,GB}$. Consequently, the total contribution of the interphase $\sigma_I \cdot f_I$ slightly decreases when the sintering temperature decreases (Figure 7(b)). This is also shown by considering the total contribution of each strengthening mechanism (Figure 7(c)). Indeed, the total contribution of the chemical gradient Σ_{grad}

is nearly constant in (HEA+Ni)-S850 and (HEA+Ni)-S600. Figure 7(c) also underlines that Σ_{GB} is not only the main contribution in each sample but also the one which increase the most from (HEA+Ni)-S850 to (HEA+Ni)-S600. This comes as no surprise since SPS is widely used for its ability to preserve small grains [40].

Knowing that, a strategy to maximize the strengthening in chemically architectured alloys can be proposed. To maintain the high value of $\sigma_{I,grad}$, a thin interphase and thus a low sintering temperature, like 500 or 600°C, is required. Meanwhile, a small grain size will advantageously be obtained. The next step is to increase the volume fraction of this thin interphase. To do so, the granulometry of the starting HEA and Ni powders should be tuned to maximize the contact area between both. One option would be to decrease the HEA powder grain size.

Table 3 : Mechanical contributions of chemically architectured alloys. σ_y and f are experimental data while the others are calculated. Details are given in the text.

Sample name	Ni contribution				HEA contribution				Interphase contribution					Total
	f	σ_{SS}	σ_{GB}	$\sigma \cdot f$	f	σ_{SS}	σ_{GB}	$\sigma \cdot f$	f	σ_{SS}	σ_{GB}	σ_{grad}	$\sigma \cdot f$	σ_y
(HEA+Ni)-S600	0,28	14	131	40	0,39	125	358	188	0,33	94	358	210	302	450
(HEA+Ni)-S850	0,18	14	68	14	0,18	125	187	57	0,64	94	187	99	382	315

f is the volume fraction of each phase, σ_X is the contribution of strengthening mechanism X, σ_y is the total yield strength. Mechanical contributions σ are in MPa.

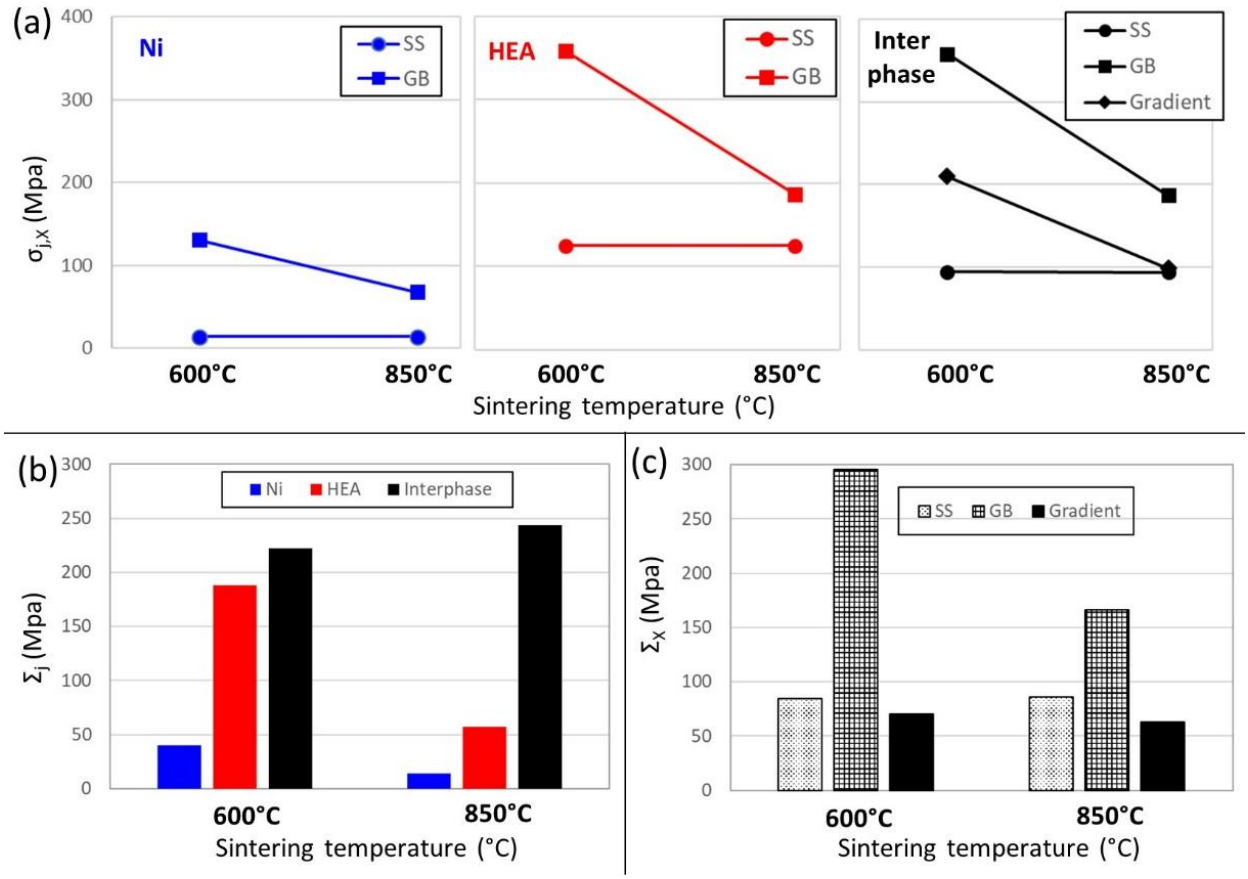

Figure 7 : Contributions to the mechanical strengthening in (HEA+Ni)-S600 and (HEA+Ni)-S850. (a) The strength of each mechanism in each phase, as defined in equation (2). (b) The total contribution of each phase as defined in equation (1) and (c) the total contribution of each mechanism as defined in equation (3).

Finally, we will discuss the origin of the strengthening induced by chemical fluctuations. The theory of strain gradient plasticity [41] introduces the notion of geometrically necessary dislocations (GND) [42] which are required to accommodate the deformation when strain gradient appears in a material. GND are stored at a specific location, *i.e.* at the place of the strain gradient, and induce a strain hardening. They were identifed as the relevant strengthening mechanism in architectured metals with bi-modal or harmonic grains [4]. A strain gradient can be generated by intrinsic elements of the microstructure. In chemically architectured alloys, the composition varies within the interphase from pure Ni to equimolar CoCrFeMnNi. Now, it was thoroughly shown that both the lattice parameter and the SSS significantly evolved with composition in single-phased alloys of the Co-Cr-Fe-Mn-Ni system [27, 28]. In the interphase, a given applied stress could generate various plastic deformation, depending on the composition, which would result in a strain gradient. To confirm this analysis, *in situ* EBSD will be performed in the future on chemically architectured HEA in order to detect possible GND.

5. Conclusion

Chemically architectured alloys are a new concept of microstructure in which two phases, here Ni and the high entropy alloy (HEA) CoCrFeMnNi, are separated by areas of continuous compositional fluctuations, which are called the interphase. Four chemically architectured alloys with varying

interphase width were processed by spark plasma sintering of a mixture of (HEA+Ni) powders. The microstructure was characterized by scanning electron microscope coupled with energy dispersive spectroscopy (EDS) and electron backscattered diffraction. Data treatment of EDS mappings permits to determine the volume fraction of interphase. The mechanical properties were measured by microhardness and compression tests. The main experimental results are the following:

- The interphase width is efficiently decreased by decreasing the sintering temperature T_{max} while increasing the sintering pressure P_{max}. Interphase width from 9.8 down to 2.4 µm is obtained with (T_{max}, P_{max}) varying from (850°C, 100 MPa) to (500°C, 600 MPa), respectively.
- The grain size and the volume fraction of the interphase also decrease when the average chemical gradient in the interphase increases.
- Hardness and yield strength increase when the sintering temperature decreases. A yield strength of 315 and 450 MPa was measured for T_{max} values of 850 and 600°C respectively. The strain hardening slightly decreases with a decrease of T_{max} but nevertheless, a significant plastic deformation is maintained.

To analyze further the evolution of the yield strength with the sintering temperature, the strengthening contributions of each mechanism in each phase were calculated. Especially, in the interphase, the solid solution strengthening was calculated by using a model previously developed for HEA. The main conclusions of those calculations are the following:

- The width and the volume fraction of the interphase are the two microstructural parameters which influence its strengthening contribution. When the width decreases and the volume fraction increases, the strengthening increases.
- In the processed materials, when the sintering temperature decreases, the interphase width decreases but so does the volume fraction. As a result, the interphase contribution remains approximately constant.
- The increase of the yield strength with the decrease of the sintering temperature is mainly due to the decrease of the grain size and the concomitant increase of the grain boundary strengthening.
- To maximize the strengthening in chemically architectured alloys, both the interphase width and the grain size should be minimized while the interphase volume fraction should be maximized. To do so, the sintering temperature should be low and the granulometry of the powder should be controlled.

In the future, new (HEA+Ni) chemically architectured alloys will be processed with an optimized microstructure in order to maximize the yield strength. Moreover, other mechanical tests, like toughness measurements or tensile tests until rupture, will be performed in order to study more precisely the ductility of chemically architectured alloys. Finally, characterizations at the nanometric scale, like transmission electron microscopy, will be performed to study further the interphase.

Acknowledgements

This work benefited from a French government grant managed by ANR in the framework of the "CAMEL" (Chemically Architectured MEtallic aLloys) JCJC project, which is coordinated by M. Laurent-Brocq.

Supplementary materials

Sample name	Interphase width (µm)					
	Co	Cr	Fe	Mn	Ni	Average
(HEA+Ni)-S500	1	2.5	2.5	3.5	2.5	2.4 ± 0.6
(HEA+Ni)-S600	2.5	3.5	3.5	4	3.5	3.4 ± 0.4
(HEA+Ni)-S700	3.5	6	6	10	6	6.3 ± 1.5
(HEA+Ni)-S850	7	10	10	12	10	9.8 ± 1.1

Table S 1 : Interphase width as determined on EDS profiles of Co, Cr, Fe, Mn and Ni through the interphase. Those five values are averaged and given in the last column. The given uncertainty is the standard deviation. The average and standard deviation are also reported ~~in~~

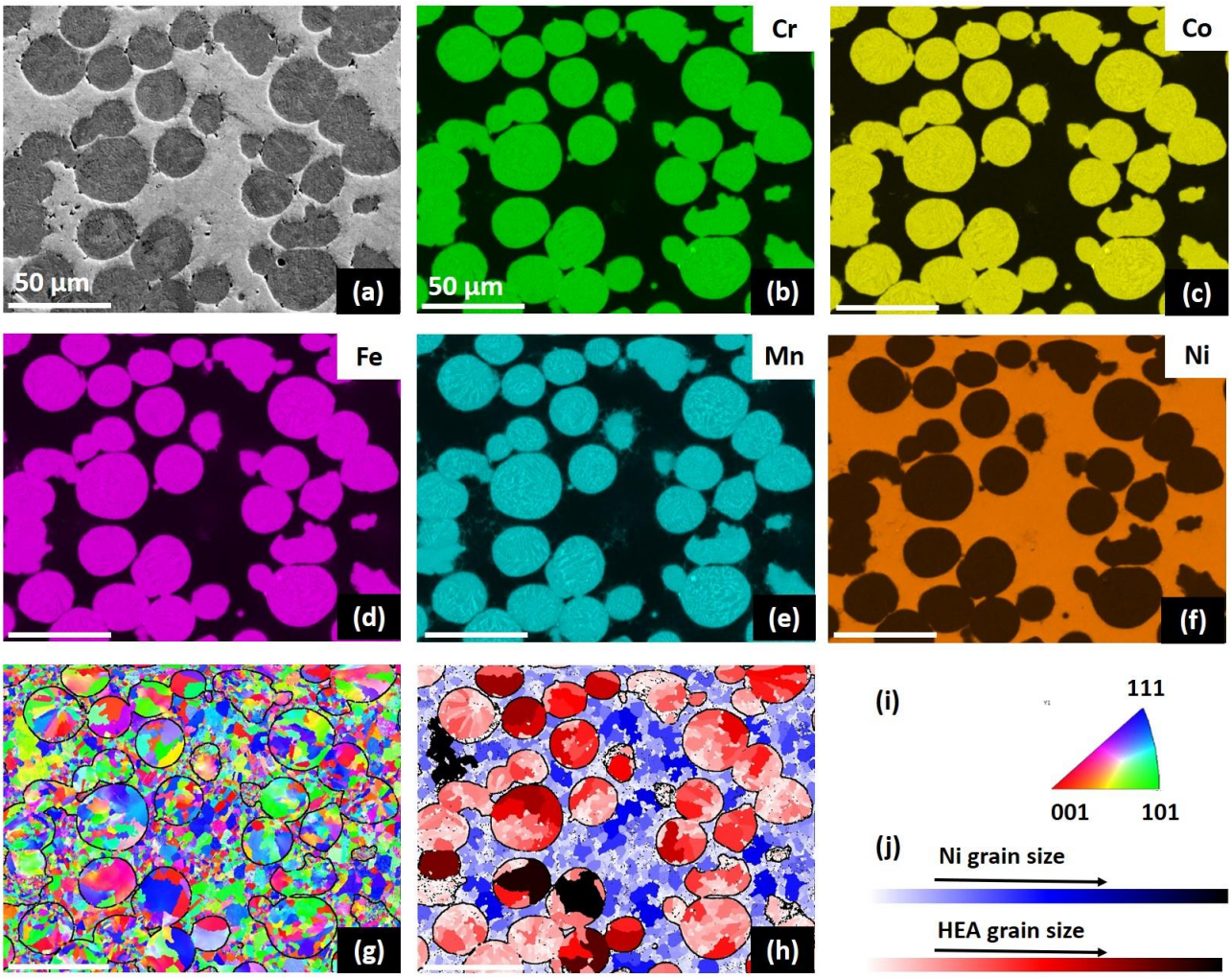

Fig. S 1 : Microstructural characterization of the chemically architectured alloy (HEA+Ni)-S500 (a) SEM image in BSE mode. (b, c, d, e and f) EDS mapping of Co, Fe, Cr, Ni and Mn respectively. (g) EBSD orientation map and grain boundaries (black lines). The corresponding standard stereographic triangle is given in (i). (g) EBSD grain size map and grain boundaries (black lines). The color legend is given in (j). The scale is the same for (b) to (h).

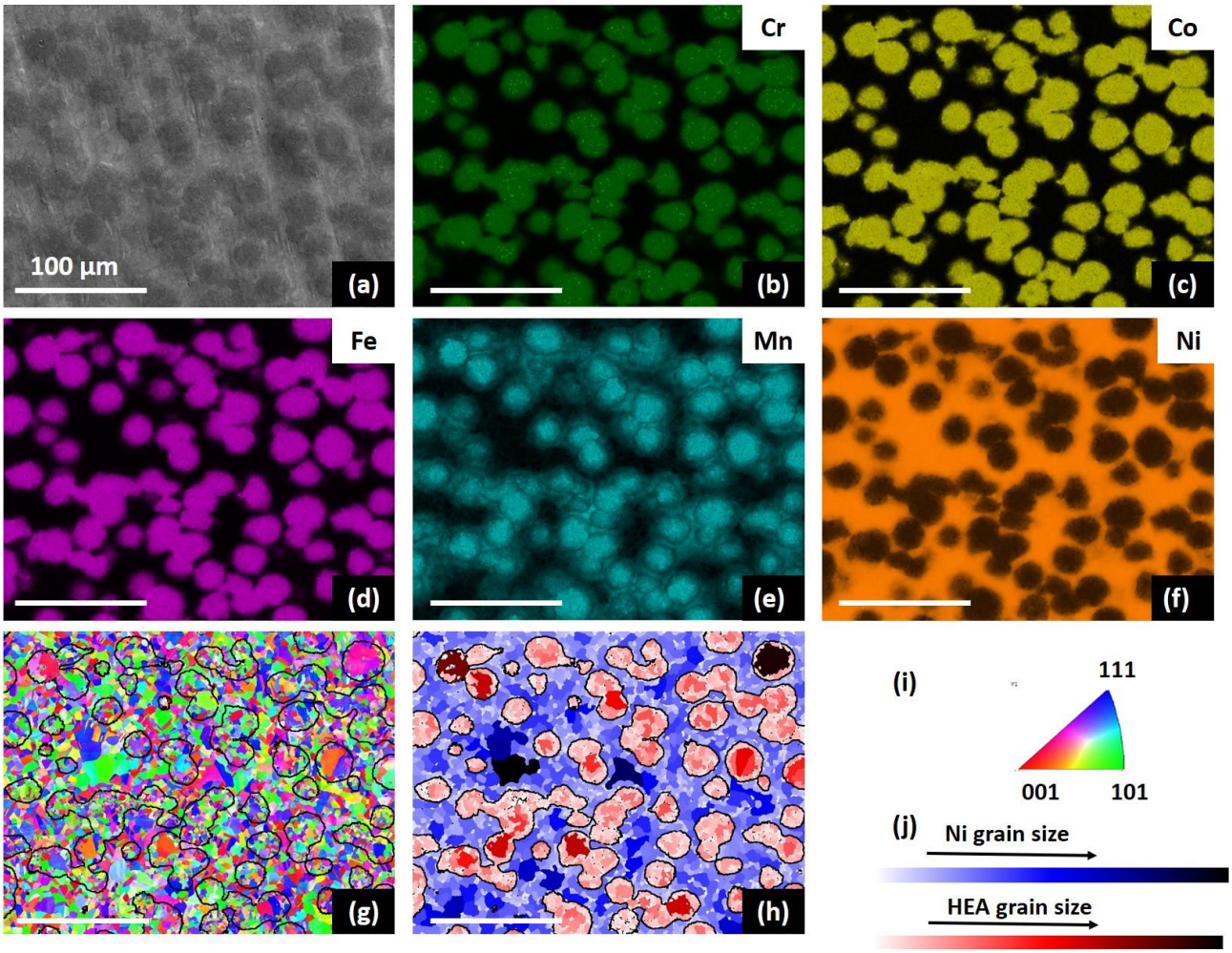

Fig. S 2 : Microstructural characterization of the chemically architectured alloy (HEA+Ni)-S700 (a) SEM image in BSE mode. (b, c, d, e and f) EDS mapping of Co, Fe, Cr, Ni and Mn respectively. (g) EBSD orientation map and grain boundaries (black lines). The corresponding standard stereographic triangle is given in (i). (g) EBSD grain size map and grain boundaries (black lines). The color legend is given in (j). The scale is the same for (b) to (h).

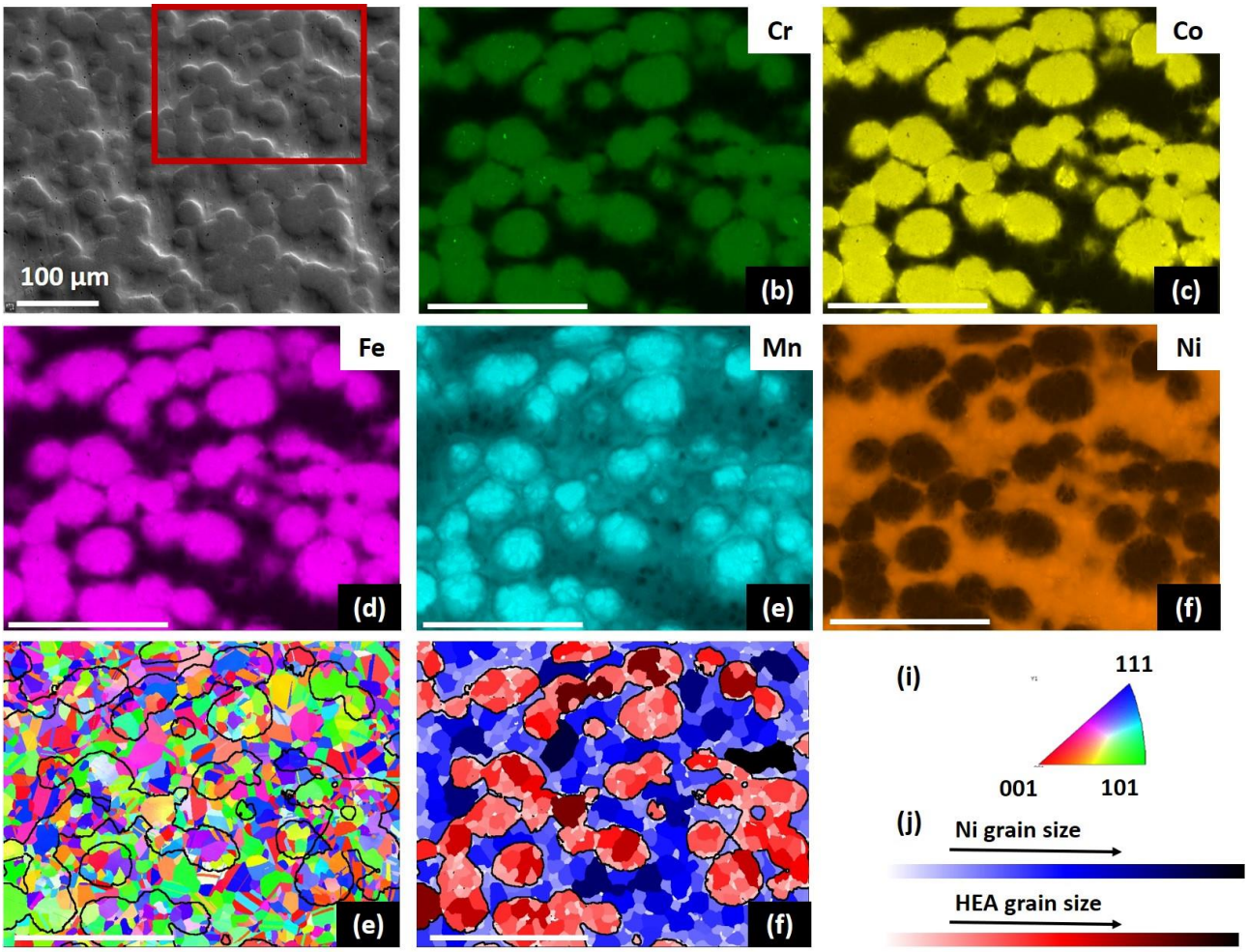

Fig. S 3 : Microstructural characterization of the chemically architectured alloy (HEA+Ni)-S850 (a) SEM image in BSE mode. The red square indicates the area of EDS and EBSD mapping. (b, c, d, e and f) EDS mapping of Co, Fe, Cr, Ni and Mn respectively. (g) EBSD orientation map and grain boundaries (black lines). The corresponding standard stereographic triangle is given in (i). (g) EBSD grain size map and grain boundaries (black lines). The color legend is given in (j). The scale is the same for (b) to (h).

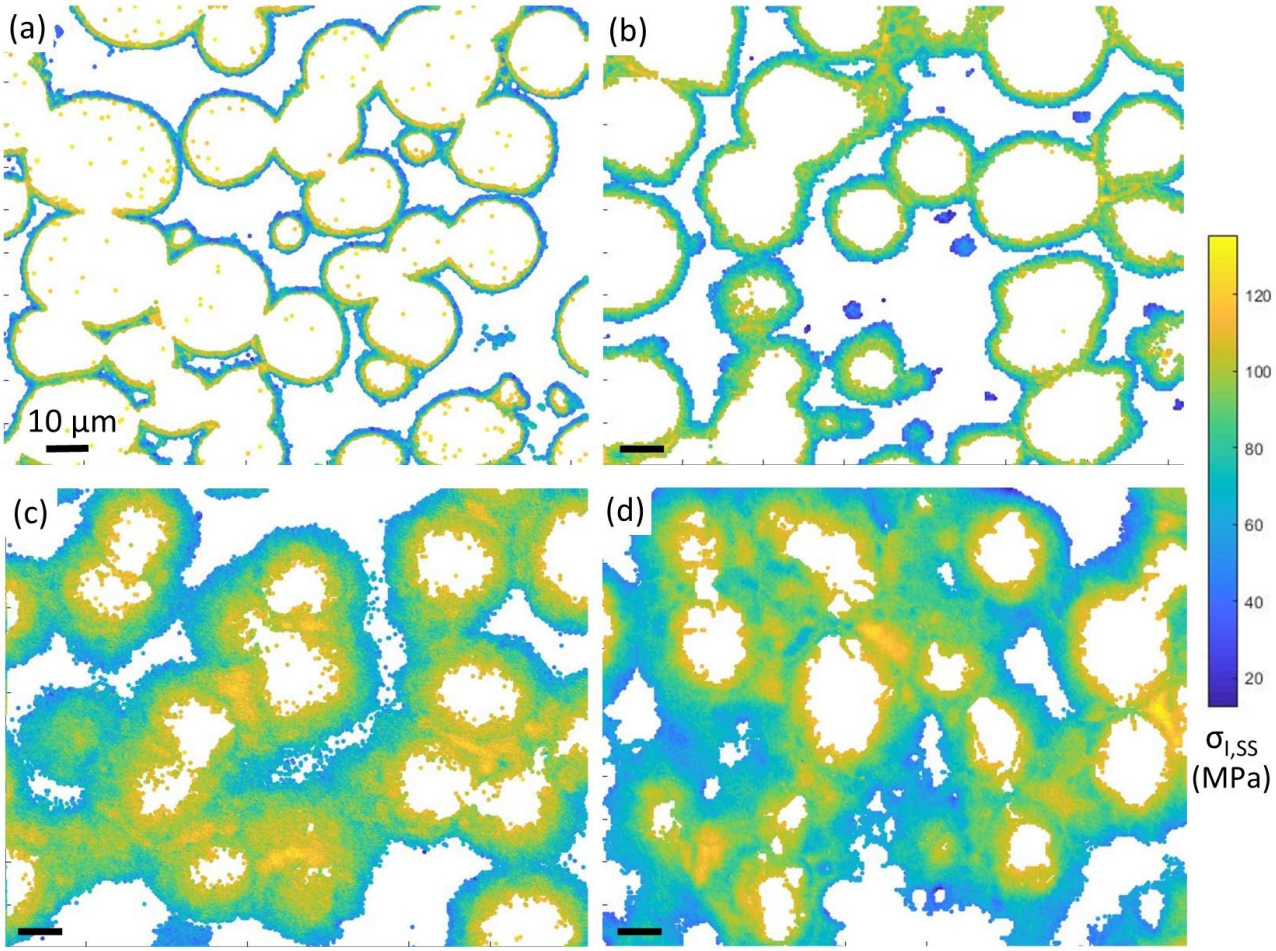

Fig. S 4 : Maps of the interphase solid solution strengthening $\sigma_{I,SS}$ for (a) (HEA+Ni)-S500, (b) (HEA+Ni)-S600, (c) (HEA+Ni)-S700 and (d) (HEA+Ni)-S850. The calculation of $\sigma_{I,SS}$ is exposed in section 4. The scale is the same from (a) to (d).

References

[1] A. Deschamps, F. Tancret, I.-E. Benrabah, F. De Geuser, H.P. Van Landeghem, Combinatorial approaches for the design of metallic alloys, C. R. Phys. 19(8) (2018) 737-754.

[2] R.O. Ritchie, The conflicts between strength and toughness, Nat. Mater. 10(11) (2011) 817-822.

[3] O. Bouaziz, Y. Brechet, J.D. Embury, Heterogeneous and architectured materials: A possible strategy for design of structural materials, Advanced Engineering Materials 10(1-2) (2008) 24-36.

[4] E. Ma, T. Zhu, Towards strength–ductility synergy through the design of heterogeneous nanostructures in metals, Materials Today 20(6) (2017) 323-331.

[5] M.F. Ashby, Y.J.M. Bréchet, Designing hybrid materials, Acta Mater. 51(19) (2003) 5801-5821.

[6] Y. Brechet, J.D. Embury, Architectured materials: Expanding materials space, Scr. Mater. 68(1) (2013) 1-3.

[7] L. Yan, Y. Chen, F. Liou, Additive manufacturing of functionally graded metallic materials using laser metal deposition, Additive Manufacturing 31 (2020) 100901.

[8] Y. Miyamoto, W.A. Kaysser, B.H. Rabin, A. Kawasaki, R.G. Ford, Functionally Graded Materials: Design, Processing and Applications, Springer, US, 1999.

[9] S. Suresh, A. Mortensen, Functionally graded metals and metal-ceramic composites: Part 2 Thermomechanical behaviour, Int. Mater. Rev. 42(3) (1997) 85-116.

[10] V. Boggarapu, R. Gujjala, S. Ojha, S. Acharya, P. Venkateswara babu, S. Chowdary, D. kumar Gara, State of the art in functionally graded materials, Composite Structures 262 (2021) 113596.

[11] B. Kieback, A. Neubrand, H. Riedel, Processing techniques for functionally graded materials, Materials Science and Engineering: A 362(1–2) (2003) 81-106.

[12] F. Lefevre-Schlick, O. Bouaziz, Y. Brechet, J.D. Embury, Compositionally graded steels: The effect of partial decarburization on the mechanical properties of spherodite and pearlite, Materials Science and Engineering: A 491(1) (2008) 80-87.

[13] V.A. Popovich, E.V. Borisov, A.A. Popovich, V.S. Sufiiarov, D.V. Masaylo, L. Alzina, Functionally graded Inconel 718 processed by additive manufacturing: Crystallographic texture, anisotropy of microstructure and mechanical properties, Materials & Design 114 (2017) 441-449.

[14] G.D. Dutel, D. Tingaud, P. Langlois, G. Dirras, Nickel with multimodal grain size distribution achieved by SPS: microstructure and mechanical properties, J. Mater. Sci. 47(22) (2012) 7926-7931.

[15] L. Farbaniec, G. Dirras, A. Krawczynska, F. Mompiou, H. Couque, F. Naimi, F. Bernard, D. Tingaud, Powder metallurgy processing and deformation characteristics of bulk multimodal nickel, Mater. Charact. 94 (2014) 126-137.

[16] M.-S. Pham, C. Liu, I. Todd, J. Lertthanasarn, Damage-tolerant architected materials inspired by crystal microstructure, Nature 565(7739) (2019) 305-311.

[17] N.A. Fleck, V.S. Deshpande, M.F. Ashby, Micro-architectured materials: past, present and future, Proceedings of the Royal Society a-Mathematical Physical and Engineering Sciences 466(2121) (2010) 2495-2516.

[18] T.Z. Xin, Y.H. Zhao, R. Mahjoub, J.X. Jiang, A. Yadav, K. Nomoto, R.M. Niu, S. Tang, F. Ji, Z. Quadir, D. Miskovic, J. Daniels, W.Q. Xu, X.Z. Liao, L.Q. Chen, K. Hagihara, X.Y. Li, S. Ringer, M. Ferry, Ultrahigh specific strength in a magnesium alloy strengthened by spinodal decomposition, Science Advances 7(23) (2021).

[19] J.A. Hanna, I. Baker, M.W. Wittmann, P.R. Munroe, A new high-strength spinodal alloy, Journal of Materials Research 20(4) (2005) 791-795.

[20] J.W. Cahn, Hardening by spinodal decomposition, Acta Metallurgica 11(12) (1963) 1275.

[21] M. Kato, T. Mori, L.H. Schwartz, Hardening by spinodal modulated structure, Acta Metallurgica 28(3) (1980) 285-290.

[22] O. Soriano-Vargas, E.O. Avila-Davila, V.M. Lopez-Hirata, N. Cayetano-Castro, J.L. Gonzalez-Velazquez, Effect of spinodal decomposition on the mechanical behavior of Fe–Cr alloys, Materials Science and Engineering: A 527(12) (2010) 2910-2914.

[23] Y. Jiazhen, L. Ning, F. Xu, Z. Ying, The strengthening effect of spinodal decomposition and twinning structure in MnCu-based alloy, Materials Science and Engineering: A 618 (2014) 205-209.

[24] M. Laurent-Brocq, D. Mereib, G. Garcin, J. Monnier, L. Perrière, B. Villeroy, Chemical architecturation of high entropy alloys through powder metallurgy, J. Alloys Compd. 835 (2020) 155279.

[25] G. Bracq, M. Laurent-Brocq, L. Perrière, R. Pirès, J.-M. Joubert, I. Guillot, The fcc solid solution stability in the Co-Cr-Fe-Mn-Ni multi-component system, Acta Mater. 128 (2017) 327-336.

[26] M. Laurent-Brocq, L. Perrière, R. Pirès, Y. Champion, From high entropy alloys to diluted multi-component alloys: Range of existence of a solid-solution, Materials & Design 103 (2016) 84-89.

[27] G. Bracq, M. Laurent-Brocq, C. Varvenne, L. Perrière, W.A. Curtin, J.M. Joubert, I. Guillot, Combining experiments and modeling to explore the solid solution strengthening of high and medium entropy alloys, Acta Mater. 177 (2019) 266-279.

[28] M. Laurent-Brocq, L. Perrière, R. Pirès, F. Prima, P. Vermaut, Y. Champion, From diluted solid solutions to high entropy alloys: On the evolution of properties with composition of multi-components alloys, Materials Science and Engineering: A 696 (2017) 228-235.

[29] M. Laurent-Brocq, X. Sauvage, A. Akhatova, L. Perrière, E. Leroy, Y. Champion, Precipitation and strength of carbonitrides in a CrMnFeCoNi high entropy alloy, Advanced Engineering Materials (2017).

[30] M. Laurent-Brocq, P.A. Goujon, J. Monnier, B. Villeroy, L. Perrière, R. Pirès, G. Garcin, Microstructure and mechanical properties of a CoCrFeMnNi high entropy alloy processed by milling and spark plasma sintering, J. Alloys Compd. 780 (2019) 856-865.

[31] E.A. Olevsky, L. Froyen, Impact of Thermal Diffusion on Densification During SPS, J. Am. Ceram. Soc. 92(1) (2009) S122-S132.

[32] J.-M. Joubert, D. Mereib, J. Monnier, B. Villeroy, L. Perrière, M. Laurent-Brocq, Use of Brinell coefficients to analyze X-ray diffraction patterns of chemically architectured alloys, in preparation.

[33] Y. Tomota, K. Kuroki, T. Mori, I. Tamura, TENSILE DEFORMATION OF 2-DUCTILE-PHASE ALLOYS - FLOW CURVES OF ALPHA-GAMMA FE-CR-NI ALLOYS, Materials Science and Engineering 24(1) (1976) 85-94.

[34] F.M. Al-Abbasi, J.A. Nemes, Micromechanical modeling of dual phase steels, International Journal of Mechanical Sciences 45(9) (2003) 1449-1465.

[35] R. Hill, Elastic properties of reinforced solids: Some theoretical principles, J. Mech. Phys. Solids 11(5) (1963) 357-372.

[36] G. Laplanche, P. Gadaud, O. Horst, F. Otto, G. Eggeler, E.P. George, Temperature dependencies of the elastic moduli and thermal expansion coefficient of an equiatomic, single-phase CoCrFeMnNi high-entropy alloy, J. Alloys Compd. 623 (2015) 348-353.

[37] F. Otto, A. Dlouhý, C. Somsen, H. Bei, G. Eggeler, E.P. George, The influences of temperature and microstructure on the tensile properties of a CoCrFeMnNi high-entropy alloy, Acta Mater. 61(15) (2013) 5743-5755.

[38] C. Keller, E. Hug, Hall–Petch behaviour of Ni polycrystals with a few grains per thickness, Mater. Lett. 62(10) (2008) 1718-1720.

[39] C. Varvenne, A. Luque, W.A. Curtin, Theory of strengthening in fcc high entropy alloys, Acta Mater. 118 (2016) 164-176.

[40] M. Yu, S. Grasso, R. McKinnon, T. Saunders, M.J. Reece, Review of flash sintering: materials, mechanisms and modelling, Adv. Appl. Ceram. 116(1) (2017) 24-60.

[41] N.A. Fleck, G.M. Muller, M.F. Ashby, J.W. Hutchinson, Strain gradient plasticity: Theory and experiment, Acta Metall. Mater. 42(2) (1994) 475-487.

[42] M.F. Ashby, Deformation of plastically non-homogeneous materials, Philos. Mag. 21(170) (1970) 399.